



# Heat conduction across irregular and fractal-like surfaces

M.G. Blyth<sup>a</sup>, C. Pozrikidis<sup>b,\*</sup>

<sup>a</sup> Department of Mathematics, Imperial College, 180 Queen's Gate, London, SW7 2BZ UK

<sup>b</sup> Department of Mechanical and Aerospace Engineering, University of California, San Diego, 9500 Gilman Dr., La Jolla, CA 92093-0411, USA

Received 1 April 2002; received in revised form 1 October 2002

## Abstract

The effect of irregularities on the rate of heat conduction from a two-dimensional isothermal surface into a semi-infinite medium is considered. The effect of protrusions, depressions, and surface roughness is quantified in terms of the displacement of the linear temperature profile prevailing far from the surface. This shift, coined the displacement length, is designated as an appropriate global measure of the effect of the surface indentations incorporating the particular details of the possibly intricate geometry. To compute the displacement length, Laplace's equation describing the temperature distribution in the semi-infinite space above the surface is solved numerically by a modified Schwarz–Christoffel transformation whose computation requires solving a system of highly non-linear algebraic equations by iterative methods, and an integral equation method originating from the single-layer integral representation of a harmonic function involving the periodic Green's function. The conformal mapping method is superior in that it is capable of handling with high accuracy a large number of vertices and intricate wall geometries. On the other hand, the boundary integral method yields the displacement length as part of the solution. Families of polygonal wall shapes composed of segments in regular, irregular, and random arrangement are considered, and pre-fractal geometries consisting of large numbers of vertices are analyzed. The results illustrate the effect of wall geometry on the flux distribution and on the overall enhancement in the rate of transport for regular and complex wall shapes.

© 2002 Elsevier Science Ltd. All rights reserved.

## 1. Introduction

The study of heat transport across the surface of a conductive medium with arbitrary geometry is of interest in a wide variety of engineering applications including the cooling of standard size and miniaturized devices in microelectronics (e.g., [1,2]). Of particular interest is the study of the effect of natural and manufactured irregularities and the identification of an optimal geometry that maximizes the overall transport rate (e.g., [3]). In most applications, because the thermal conductivity is large or the characteristic length scale of interest is small, the Peclet number is high, conduction dominates con-

vection, and the temperature field satisfies Laplace's equation to leading order approximation.

One convenient model for studying the effect of surface geometry is provided by an isothermal boundary containing a large number of finite-size or microscopic, regular or random indentations. Transport occurs into a semi-infinite conducting medium lying on one side of the boundary, and is driven by a temperature gradient imposed far from the boundary. In practice, the temperature gradient may be induced by a cooling stream or liquid film or by the presence of another isothermal surface placed above the irregular surface. The aim of the analysis is to assess the influence of the surface depressions, protrusions, or roughness on the rate of transport relative to that prevailing in the absence of the irregularities.

In the case of a virtually infinite rough or periodic surface, the effect of the irregularities can be quantified in terms of the displacement of the linear temperature

\* Corresponding author. Tel.: +1-858-534-6530; fax: +1-858-534-7078.

E-mail address: [cpozrikidis@ucsd.edu](mailto:cpozrikidis@ucsd.edu) (C. Pozrikidis).

profile prevailing far from the surface. If the surface is perfectly smooth, the displacement length vanishes, as required by the designation of the reference shape. This measure of enhancement may also be used to characterize a non-periodic surface of finite extent as well as a smooth surface containing solitary projections or depressions, provided that the periodic extension is considered. The displacement length provides us with an unambiguous as well as convenient global measure of the effect of the possibly intricate microstructures without explicit reference to the particulars of the geometry.

To illustrate the usefulness of the displacement length, consider heat conduction from an infinite isothermal surface whose profile is described by the equation  $y = H(x)$ , where  $H$  is a periodic function of  $x$ , with transport occurring into the upper half plane. The temperature field at steady state satisfies Laplace's equation  $\nabla^2 T = 0$ , subject to the boundary condition that  $T = T_0$  over the surface, and  $\partial T / \partial y \rightarrow -q/\kappa$  far from the surface, where  $q$  is a specified constant flux, and  $\kappa$  is the thermal conductivity. In the case of a flat surface located at  $y = H(x) = 0$ , the solution is readily found by inspection to be  $T = T_0 - qy/\kappa$ . For non-flat periodic geometries, the temperature field in the vicinity of the surface and the distribution of flux over the rough surface are non-trivial to calculate. In all cases, however, as  $y \rightarrow \infty$ , the temperature profile exhibits the asymptotic behavior  $T \sim T_0 - q(y - l)/\kappa + \text{edt}$ , where  $l$  is the displacement length and edt stands for exponentially decaying terms. If the far field flux condition is replaced with the requirement that  $T = T^\infty$  over a flat surface located at  $y = d$ , where  $d$  is large enough to allow the asymptotic behavior to be established, the flux is given by

$$q = -\frac{\kappa}{1 - l/d} \left( \frac{T^\infty - T_0}{d} \right). \quad (1)$$

If the displacement length  $l$  is positive (negative), the factor  $(1 - l/d)^{-1}$  represents an increase (decrease) in heat flux in the presence of the crenulations.

In the Appendix A, it is shown that the displacement length reaches an absolute maximum in the limit as the irregularities become dense, yielding a coated surface with a uniformly shifted profile. In particular applications, however, geometrical and other manufacturing restrictions will not make this choice acceptable, and non-dense profiles are considered. Fyrrillas and Pozrikidis [4] recently computed the displacement length for a doubly-periodic three-dimensional surface with sinusoidal corrugations of arbitrary height and wave length using asymptotic and numerical methods. The main objective of the present study is to illustrate the magnitude of the displacement length for complex and pre-fractal families of two-dimensional surfaces, and thereby

demonstrate the precise effect of an intricate wall geometry on the enhancement in the overall transport rate.

Wall roughness in two dimensions may be simulated by considering polygonal periodic profiles. For this family of shapes, detailed crenulations may be constructed by introducing an increasingly high number of vertices at random or recursively computed positions. Flat surfaces containing simple symmetrical asperities were considered by Taylor [5] and Richardson [6] in their studies of viscous flow along a periodically indented wall. Following a proposition by Mandelbrot [7], fractal models have been used to mimic natural surface rugosity, and the results provided scaling laws and quantitative predictions (e.g., [8,9]). Random irregularities and pre-fractal surfaces will also be considered in the present study.

In the case of two-dimensional conduction, complex-variable theory provides us with an expeditious venue for computing analytical and numerical solutions. In particular, conformal mapping allows us to map the irregular domain of solution in physical space onto the upper-half mapped plane wherein a simple solution for the problem under consideration is available. A suitable mapping for periodic geometries may be constructed by modifying the classical Schwarz–Christoffel transformation, as discussed by Floryan [10,11] who extended the methods of Davis [12] for coordinate grid generation. Owen and Blatt [13] used the modified Schwarz–Christoffel mapping to study flow over a wall with rectangular depressions and curved tops.

To derive the Schwarz–Christoffel transformation, the wall vertices must be mapped from their natural location in the physical plane to new locations along the real axis of the transformed plane. The mapped locations themselves appear implicitly in the conformal mapping function. We shall demonstrate that, for the very simple case of a periodic wall composed of triangular asperities, the mapped locations can be written down immediately based on global constraints involving the vertex turning angles. In general, however, the mapped locations must be computed using iterative methods. One advantage of the conformal mapping formulation is that the cumulative heat transport rates along the wall from an arbitrary point up to the physical wall vertices is proportional to the difference between the mapped vertex locations. This feature circumvents the computation of the rate of transport by finite difference approximations, and thereby prevents the introduction of further numerical error.

In the case of a periodic wall consisting of linear segments, the conformal mapping is expressed in terms of an infinite product that must practically be truncated at a finite level. For the semi-infinite domain presently considered, this truncation level is restrictively high, leading to significant inaccuracies. In contrast, when the solution domain is an infinite strip, the truncation level

is proportional to the separation between the two confining surfaces, and truncation at a moderate level is permissible. In Section 2, we shall show that the infinite product can be expressed in closed form, thereby eliminating an important source of error.

To provide a check on the accuracy of results obtained by the conformal mapping method, and also demonstrate an alternative method of computation, we formulate the solution using the boundary-integral method. In this method, the temperature field is expressed in terms of a surface distribution of periodic Green’s functions constituting a single-layer harmonic potential. Although this formulation is more versatile in that it can handle arbitrarily shaped boundaries, it is practically limited by high computational cost placing restrictions on geometrical complexity. One advantage of the boundary-integral method is that it furnishes the displacement length as part of the solution of an integral equation for the surface flux distribution.

A useful analogy can be made between the problem of heat conduction presently considered and the problem of shear flow over a dense, perforated, or porous wall [14]. In the case of unidirectional flow along a cylindrical wall, the fluid velocity satisfies Laplace’s equation with the no-slip condition required over a solid surface and the zero shear stress condition required far below a perforated or porous surface. In all cases, the shear rate approaches a specified value a long way above the surface, and a slip velocity that is analogous to the temperature displacement length  $l$  is established over the surface. Our results for the heat conduction problem may thus be interpreted directly in the context of hydrodynamics.

## 2. Numerical methods

We consider Laplace’s equation for the temperature distribution in a two-dimensional semi-infinite domain lying above an isothermal periodic wall with polygonal shape. The solution will be computed by two complementary methods involving conformal mapping and a representation in terms of a boundary distribution of point-source dipoles.

### 2.1. Conformal mapping

In the conformal mapping method, the actual solution domain is projected to the upper half plane using a suitably adapted version of the Schwarz–Christoffel transformation. An analytic function can then be found in the mapped plane that satisfies properly transformed boundary conditions. In the present case, the Dirichlet boundary condition along the wall is preserved by the transformation, and the main difficulty lies in calculating the particular details of the transformation.

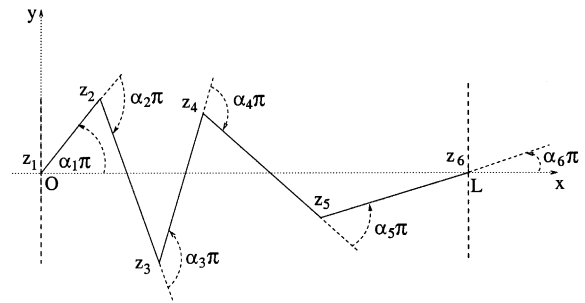


Fig. 1. A typical wall period of length  $L$  with  $N = 6$  vertices. The wall is repeated periodically along the  $x$ -axis.

Consider a wall composed of straight line segments with  $N$  vertices, as shown in Fig. 1. Extending the work of Floryan [11] and Davis [12], we find that the transformation mapping a piecewise-linear wall from the physical  $z = x + iy$  plane onto the  $\zeta = \xi + i\eta$  plane has the differential form

$$\frac{dz}{d\zeta} = R \prod_{j=1}^N \prod_{k=-\infty}^{\infty} (\zeta - kL - a_j)^{\alpha_j}, \tag{2}$$

where  $R$  is a complex constant,  $a_j$ , for  $j = 1, \dots, N$ , are the image points of the physical wall vertices  $z_j$  located on the  $\xi$ -axis, and  $\pi\alpha_j$  are the turning angles from one wall segment to the next, as illustrated in Fig. 1. The infinite  $k$  product represents the contributions from all periods. The angles are taken to be positive if the turning is clockwise, and negative otherwise. The first and last turning angles are measured with respect to the  $x$ -axis. Appropriate branch cuts are made in the lower half  $\zeta$ -plane to ensure that the right hand side of (2) is a continuous, single-valued, function over the domain of interest, which is the upper-half plane. Since the wall is periodically repeated, as shown in Fig. 1, the turning angles over a single period add up to zero,

$$\sum_{j=1}^N \pi\alpha_j = 0. \tag{3}$$

The second product in Eq. (2) with respect to  $k$  maps a repeated wall of period  $L$  onto the real line in the  $\zeta$ -plane.

According to Riemann’s mapping theorem (e.g., [15]), a unique transformation can be specified by requiring that three arbitrary points in the  $z$ -plane are mapped onto three chosen points in the  $\zeta$ -plane. The remaining coefficients  $a_j$  are fixed by the transformation. Following Floryan [10,11], we demand that the origin in physical space map onto the origin in the transformed space, and further insist that the point  $z_N = L$  be mapped onto the point  $a_N = 1$ . The selection of the third arbitrary point, identified with the degenerate corner at

infinity in the upper-half  $z$ -plane, is implicit in the nature of the transformation.

Floryan [10] showed that, in the case of a strip- or channel-like solution domain, the infinite product in (2) can be truncated at very few terms without significant loss of accuracy. Truncation can also be performed in the case of a semi-infinite domain, but the truncation level must be raised as the transformation is evaluated at increasingly large distances from the wall. This difficulty can be entirely circumvented by use of the identity

$$\sin(\pi z) = \pi z \prod_{k=1}^{\infty} (1 - z^2/k^2), \tag{4}$$

(e.g., [16]), which can be used to reduce (2) to the simplified form

$$\frac{dz}{d\zeta} = R \prod_{j=1}^N \{\sin \pi(\zeta - a_j)/L\}^{\alpha_j}. \tag{5}$$

Upon integration, we obtain the relationship

$$z = R \int_0^{\zeta} g(\zeta') d\zeta', \tag{6}$$

where  $g(\zeta)$  is the product on the right hand side of (5). When  $\zeta = a_N = 1$ , the integral in (6) is equal to unity, as may readily be shown using contour integration. Thus, in order that  $z_N = L$ , it must be  $R = L$ . This realization is a further departure from Floryan’s formulation [11] who treated  $R$  as an unknown to be computed as part of the solution. Moreover, performing the integration in (6) along the contour  $\zeta = \xi_0$ , where  $0 < \xi_0 < 1$ , we find that, to be able to satisfy the far field condition, the identity

$$\sum_{j=1}^N \alpha_j a_j = 0 \tag{7}$$

must hold for any wall with  $N$  vertices. We shall see later in this section that this identity can be used to derive an exact analytical solution for a wall with a saw-tooth profile.

With the transformation (6), the solution of the original problem becomes a simple matter in the  $\zeta$ -plane. For any analytic complex function,  $w = \psi(\zeta, \eta) + iT(\zeta, \eta)$ , the real and imaginary parts together satisfy the Cauchy–Riemann equations, and are thus harmonic functions. The solution satisfying the Dirichlet wall condition and far-field condition in our case is simply  $w = -qL\zeta/\kappa + iT_0$ , and so  $\psi = -qL\zeta/\kappa$  and  $T = -qL\eta/\kappa + T_0$ , where  $q$  is the flux far from the wall. The satisfaction of the far-field condition can be confirmed by taking the limit  $\zeta \rightarrow \infty$  in (5), and recalling that the sum of the turning angles is zero.

The rate of heat transport across the wall follows immediately once the transformation is known. In particular, the integrated flux or cumulative rate of trans-

port across the wall from the origin up to an arbitrary point  $A$  is given by the expression

$$q_A = -\kappa \int_0^A \frac{\partial T}{\partial n} ds = -\kappa \int_0^A \frac{\partial \psi}{\partial s} ds = qL\xi_A, \tag{8}$$

where  $\partial/\partial n$  and  $\partial/\partial s$  are the normal and tangential derivatives with respect to distance normal to or along the physical wall, respectively,  $ds$  is the differential arc length along the wall, and  $\xi_A$  is the image of the point  $z = A$  in the  $\zeta$ -plane. The cumulative rate of transport corresponding to each vertex is thus proportional to the vertex location along the  $\zeta$ -axis, and the total transport rate over a single period is equal to  $qL$ , consistent with the far field condition  $\partial T/\partial y \rightarrow -q/\kappa$ .

The displacement length  $l$  is found by integrating the differential Eq. (2) with respect to  $\eta$  along a line of fixed  $\zeta$ , starting from an arbitrary point along the  $\zeta$  axis and subtracting the linear part of the solution. Correspondingly, the dimensionless displacement constant  $c_D \equiv l/L$  is calculated using the formula

$$c_D = i \int_0^{\infty} [g(\zeta_0, \eta) - 1] d\eta, \tag{9}$$

where the location  $\zeta_0$  is arbitrary. Integrating Eq. (2) along lines of constant  $\eta$  produces isotherms in the physical plane.

Consider a wall with a saw-tooth profile (corresponding to  $N = 3$ ) of height  $h$ , where each period in physical space contains three vertices located at  $z_1 = 0$ ,  $z_2 = X + ih$ ,  $z_3 = L$  mapped at the vertices  $a_1 = 0$ ,  $a_2 = \Xi$  and  $a_3 = 1$ . In this case, for a given value of  $X$ , the value of  $\Xi$  follows immediately from the constraint Eq. (7) and the knowledge of the turning angles. For an isosceles triangle ( $X = L/2$ ), we therefore find that  $\Xi = 1/2$  for any  $h$ . For a non-periodic wall with a single triangular protrusion, the form of the conformal mapping is a standard textbook exercise involving beta functions. Interestingly, constraint (7) provides no new information for the mapped vertices of a wall containing symmetric triangular asperities corresponding to  $N = 5$ , as shown in Fig. 2, but reduces instead to a verifiable statement about the vertex turning angles. For non-symmetric wall profiles, the constraint reduces the number of unknowns by one unit and is thus of little practical value.

Determining the mapping of the vertices in the physical plane to those in the transformed plane in the general case requires solving a system of highly non-linear equations, and this poses a substantial problem, not least because of the way in which the mapped vertices appear inside the transformation. For practical purposes, the solution must be found numerically using a suitable means of iteration.

We have implemented a scheme similar to that developed by Floryan [11]. The known variables are the  $N$

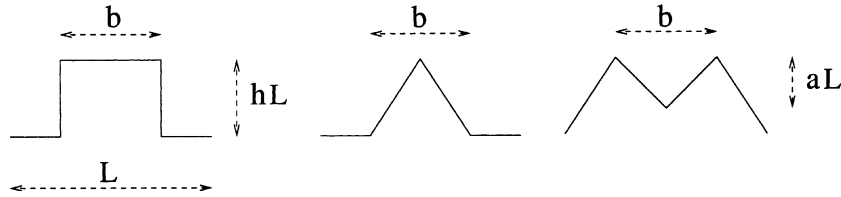


Fig. 2. Illustration of regular (non-random) symmetric protrusions (not drawn to scale). In each case, the width of the asperity is  $b$  and the period is  $L$ . From the left, the heights are  $h = \sqrt{3}/2, \sqrt{3}/2, 8.0$  respectively. For the M-shaped wall,  $a = h(1 - b/L)$ , where  $h$  is the maximum height of the protrusions.

wall vertices  $z_j$  and associated turning angles  $\pi\alpha_j$ , and the unknowns are the locations of the wall vertices in the transformed plane,  $a_j$ . Although these vertices should all lie on the real  $\xi$ -axis, they are assumed to be complex in the implementation. The iteration procedure involves the following steps: (1) Make guesses for  $a_j$ ; (2) compute estimates for the wall nodes in physical space,  $\hat{z}_j$ , according to the transformation (6); (3) adjust the guesses for the  $a_j$  using the correction formula

$$|a_j - a_{j-1}| = \mu |\hat{a}_j - \hat{a}_{j-1}| \frac{|z_j - z_{j-1}|}{|\hat{z}_j - \hat{z}_{j-1}|}, \quad (10)$$

where  $\hat{a}_j$  are the most recent estimates of the exact values of  $a_j$  available from the previous iteration, and the parameter  $\mu$  is chosen at each sweep to ensure  $a_N = 1$ . The procedure is repeated until the  $a_j$ 's have converged to within a prescribed tolerance. In practice, for most of the wall shapes considered, initial guesses for the  $a_j$ 's evenly spaced between 0 and 1 are sufficient to ensure convergence.

In the numerical implementation, the Schwarz–Christoffel integrals are evaluated using the 20-point Gauss–Legendre quadrature (e.g., [17]). To ensure high accuracy, the singularities due to the negative turning

angles are subtracted out and integrated exactly. The displacement length is evaluated by integrating along a line of constant  $\xi$  up to a large enough  $\eta$ . Numerical testing confirmed that the converged locations of the vertices are independent of the starting point within the quoted accuracy. We found that, for the most complicated wall shapes considered, the numerical method is sufficient to achieve an accuracy of four decimal places or better in the computation of the displacement length, provided that the convergence tolerance is sufficiently low. For small values of the number of vertices  $N$ , in the range 10–20, the whole calculation takes only a few seconds, but the cost quickly escalates as  $N$  is raised. Fig. 3 shows the rate of convergence for two cases, the third and second iterates of the Von Koch and Minkowski curves, respectively, both to be discussed in Section 3. The error at the  $n$ th iteration is measured as  $e(n) = \sum_{j=1}^N (z_j - \hat{z}_j)^2$ . It is clear from the two plots that the rate of convergence is linear.

### 2.2. Double-layer representation

A competitive alternative to the conformal mapping method is provided by the double-layer representation

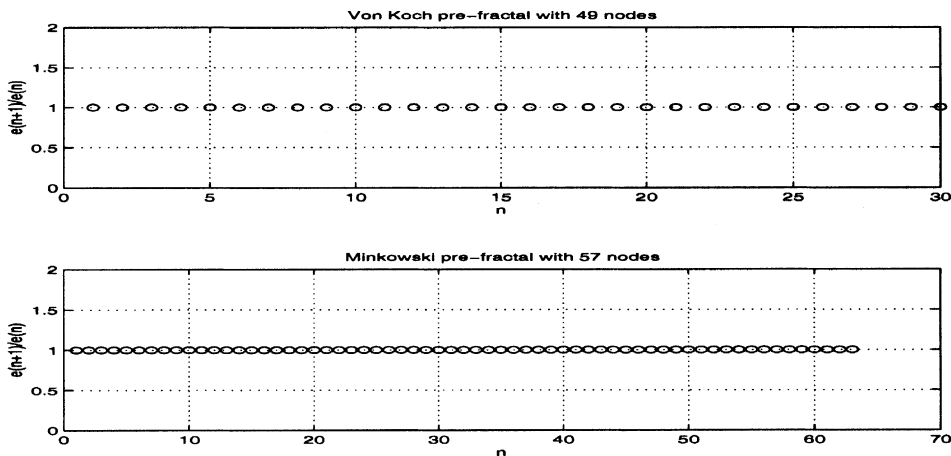


Fig. 3. Rate of convergence for (top) the third iterate Von Koch curve with 49 nodes, and (bottom) the second iterate Minkowski curve with 57 nodes. In both cases,  $e(n)$  denotes the error after the  $n$ th iteration.

(e.g., [18]). In this formulation, the temperature at the point  $\mathbf{x}_0 = (x_0, y_0)$  that lies in the physical domain of solution is expressed in the integral form

$$T(\mathbf{x}_0) = T_0 + \frac{1}{\kappa} \int_C G(\mathbf{x}, \mathbf{x}_0) f(\mathbf{x}_0) dl(\mathbf{x}) - \frac{q}{\kappa} (y_0 - l), \quad (11)$$

where  $C$  is one period of the wall and  $l$  is the a priori unknown displacement length.  $f = -\kappa \mathbf{n} \cdot \nabla T$  is the heat flux at the wall,  $\mathbf{n}$  is the unit vector pointing into the solution domain, and  $G$  is the singly-periodic upward-biased Green's function of Laplace's equation available in closed form [14]. A thermal energy balance requires the integral constraint

$$\int_C f dl = qL, \quad (12)$$

which can be regarded as the counterpart of relation (8).

Writing the integral representation (11) at a point  $\mathbf{x}_0$  located at the periodic wall, and enforcing the boundary condition  $T = T_0$ , we obtain an integral equation of the first kind for the wall flux  $f$ ,

$$\int_C G(\mathbf{x}, \mathbf{x}_0) f(\mathbf{x}_0) dl(\mathbf{x}) = q(y_0 - l), \quad (13)$$

supplemented by the integral constraint (12). To compute the solution, we discretize one period of the wall into a collection of boundary elements, and approximate the wall flux  $f$  with a constant function over each element. Applying the integral equation at the mid-point of each element provides us with a system of linear equations for the constant values of the flux. The linear system is solved by the method of Gauss elimination, and the displacement length  $l$  is obtained directly as part of the solution. The values of  $c_D \equiv l/L$  calculated in this way with 32 boundary elements along each wall segment are correct to three significant figures.

### 3. Results

Our main objective is to quantify the effect of wall roughness on the rate of transport in terms of the dimensionless displacement constant  $c_D$ . In the numerical studies, we consider simple regular wall shapes, and then more complex fractal-like and random patterns. All results presented in Sections 3.1–3.4 were obtained by the conformal mapping method discussed in Section 2.1. Results obtained by the double-layer representation are discussed in Section 3.5.

A theorem of geometrical inclusion states that the rate of transport across any surface of constant  $\eta$  is higher than that across any other such line which it physically encloses from above. The proof can be adapted to show that the value of  $c_D$  for a given wall

must be less than that for any wall which encloses the given wall from above, as discussed in the Appendix A. Consequently, the value of  $c_D$  is bounded from above by the maximum wall height. If the maximum and minimum heights of a specified wall are  $h_1 L$  and  $-h_2 L$ , respectively, where  $h_1$  and  $h_2$  are positive dimensionless coefficients, then it follows that  $-h_2 \leq c_D \leq h_1$ . More general theorems of geometrical inclusion are available in the literature (see, for example, [19]).

#### 3.1. Simple protrusions

The simplest example is the saw-tooth wall with triangular asperities considered earlier in Section 2. For certain special values of the angles subtended by the triangle sides, the displacement coefficient  $c_D$  can be computed exactly by analytical methods. For example, if  $\alpha_2 = \pm 2/3$ , corresponding to an equilateral triangle, we find  $c_D = \sqrt{3}/4 + 3 \log(3)/4\pi$ , which agrees to seven decimal places with the numerically calculated value.

Next, we investigate the three regular (i.e. non-random) symmetric asperities presented in Fig. 2. Fig. 4 shows a graph of  $c_D$  plotted against the ratio of the asperity width to wave length,  $b/L$ , with  $h$  held constant. As the ratio  $b/L$  is increased, the rectangular pulse changes continuously from a flat wall of height  $h = \sqrt{3}L/2$ , whereupon  $c_D = h$ , to an infinite sequence of periodic spikes of height  $h$ . The triangular pulse changes smoothly from a saw-tooth wall, for which  $c_D = 0.6952$  by the previous analysis, to a sequence of periodic spikes of height  $h$ . The numerical method fails to converge to within an acceptable accuracy when the triangular protrusion width approaches unity, due to the increasing proximity of the two vertices at the left hand end.

While the surface length is constant for the rectangular pulse, it is reduced by about 27% for the triangular pulse when  $b/L$  is changed from zero to unity. The corresponding changes in  $c_D$  are 33% for the rectangular pulses, and 7% for the triangular pulses. Both protrusions have the same constant height, each beginning as a spike at  $b/L = 0$  with the same surface length. It would appear therefore that significant differences in  $c_D$  are due predominantly to changes in shape rather than an appreciable increase in surface area. Although it is not clear what the most important factor is, we do see in this example that a significant reduction in surface length leads to a much smaller variation in the size of the displacement constant.

In both of the previous two cases, the displacement constant varies monotonically with the asperity width. A slightly artificial example may be constructed in which the dependence is non-monotonic. Consider the M-shaped pulse shown in Fig. 2. If we set  $a = h(1 - b/L)$  and  $h = 8$ , then zero asperity width corresponds to a symmetric saw-tooth wall for which  $c_D = 7.7846$ , while

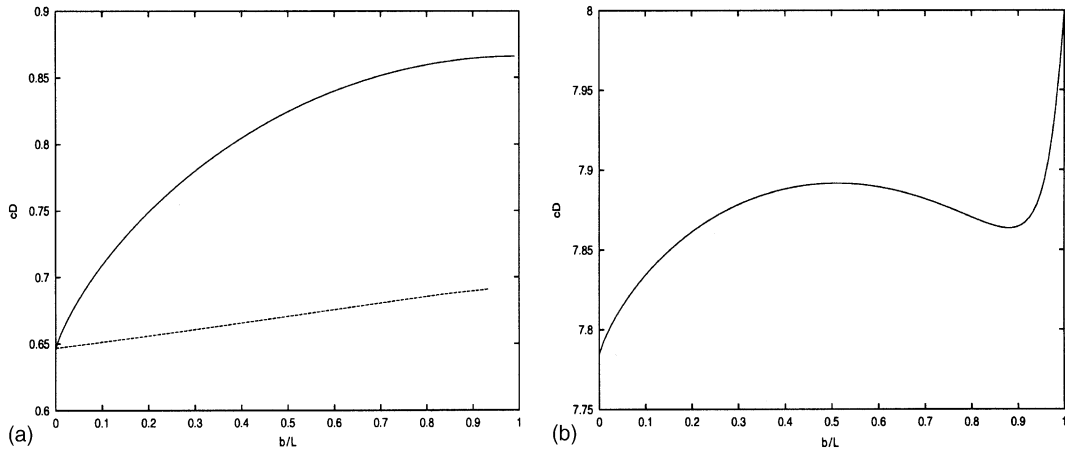


Fig. 4. Displacement constant  $c_D$  for various asperity widths  $b$  for the shapes shown in Fig. 2. (a) The solid and dashed lines are for the rectangular and triangular pulses, respectively, both with a fixed height of  $\sqrt{3}/2$ . The curve for the triangular pulse stops short of  $b/L = 1$  due to convergence difficulties. (b) M-shaped wall with height  $h/L = 8$ .

unit asperity width gives a flat wall with  $c_D = 8$ . In this case, as  $b/L$  is raised, the curve is no longer monotonic but develops instead a local minimum, as shown in Fig. 4(b).

### 3.2. Von Koch fractal shapes

The effects of true wall roughness can be simulated by considering more intricate wall designs. A convenient starting point is the fractal wall provided by the Von Koch snowflake curve (e.g., [20]). This is constructed beginning with a straight line segment of length  $3L/2$ , removing the middle third, and replacing it with an equilateral triangular hump so that the length of all segments is equal. The action is then performed on the individual new segments, and the whole process is repeated ad infinitum to produce the fractal. In the present implementation, the curve is truncated to represent a single period of a periodically repeated wall. After  $m$  iterations, where  $m = 0$  refers to the initial straight segment, the total surface length of the truncated curve is equal to  $(3L/2)(4/3)^{m-1}$ , which diverges as  $m \rightarrow \infty$ . For large  $m$ , we are able to consider highly crinkly walls with large surface areas. The wall corresponding to the discretization level  $m = 4$  described by 193 vertices is shown in Fig. 5(a) along with lines of constant temperature. As the number of vertices is increased, the calculation takes a prohibitively long time, and we were able to consider shapes only up to, and including, the iteration number  $m = 5$  involving 769 vertices.

Results for the displacement constant  $c_D$  are summarized in Table 1. The maximum height of the fractal line is  $\sqrt{3}L/4 = 0.4330L$ , independent of  $m$ . Accordingly,  $c_D$  is bounded from above by  $h_{\max} = \sqrt{3}/4$  at all fractal iterations. As the intricacy of the indentations increases,  $c_D$  grows, albeit at a monotonically decreasing rate.

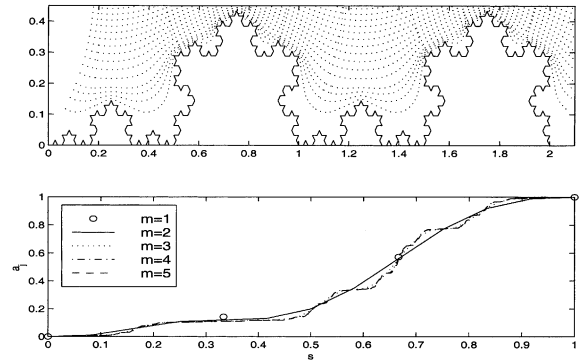


Fig. 5. Numerical solutions for the Von Koch pre-fractals. Top: The Von Koch curve for  $m = 4$  with equally-spaced temperature contours. Bottom: Dimensionless cumulative transport rates,  $a_j$ , at each vertex,  $j = 1, \dots, N$  plotted against the cumulative arc length along the curve normalized by the total arc length.

Although the surface length increases by a third after each iteration, the percentage change in  $c_D$  from one iteration to the next decreases quite sharply, until the change from  $m = 4$  to 5 is only 0.6%. For  $m = 5$ ,  $c_D$  is about 73% of  $h_{\max}$ . According to our earlier discussion, as  $m \rightarrow \infty$ ,  $c_D$  is expected to approach a limit that is lower than  $h_{\max}$ . The bracketed numbers in Table 1 are the percentage ratios of the displacement constant to its corresponding value for a horizontal flat wall which rests just on top of the fractal. The cumulative transport rates at the vertices are plotted in Fig. 5(b) for each of the five iterates. Recall that the total heat flux across the wall is fixed by the far field condition. As a consequence, each of the curves reaches unity at the final vertex.

Table 1  
Summary of calculated values of  $c_D$ ; the values of  $c_D$  for different iterates,  $m$ , of the various periodic fractal-like walls

Iteration number $m$	$c_D$ Von Koch	$c_D$ Minkowski	$c_D$ Minkowski island
1	0.2654 (61.29)	0.2591 (77.73)	0.1103 (44.12)
2	0.2970 (68.58)	0.3014 (72.34)	0.1422 (56.88)
3	0.3104 (71.68)	–	0.1550 (55.12)
4	0.3152 (72.79)	–	0.1600 (56.89)
5	0.3173 (73.27)	–	0.1620 (56.82)

The bracketed numbers give  $c_D$  as a percentage of its maximum possible value, corresponding to a horizontal flat wall which just touches the top of the fractal.

3.3. Minkowski and other fractal shapes

Other fractal-like shapes can be constructed by working in a similar fashion: begin with a specific piecewise-linear motif, replace each straight segment with a scaled-down version of that same design, and repeat in perpetuum (e.g., [20]). Here, we consider two further examples whose basic motifs are displayed in Fig. 6. In the numerical studies, each motif is iterated to create a pre-fractal shape representing a single period of a repeating wall. Typical computed temperature contours are shown in Figs. 7 and 8 along with the cumulative transport rates at the vertices. Values of the displacement constant  $c_D$  are summarized in Table 1. Note that the computations for the  $m = 3$  basic Minkowski curve described by 449 nodes, fails to converge probably due to insufficient numerical precision.

The height of the Minkowski island fractal increases slightly with successive iterates, while the surface length rises by 41% after each iteration. The percentage change in the displacement constant drops quite sharply, reaching only a 1% difference between the fourth and the fifth iterates. These results are consistent with our experience that, beyond a certain point, the introduction of an increasingly fine wall structure has little effect on the overall transport rate. This viewpoint is also reflected in the crowding of the individual transport rates,  $a_j$ , as  $m$  increases in Fig. 8. It is interesting to observe that the variation of the bracketed numbers in Table 1, representing the percentage ratios of the displacement constant to its corresponding value for a horizontal flat

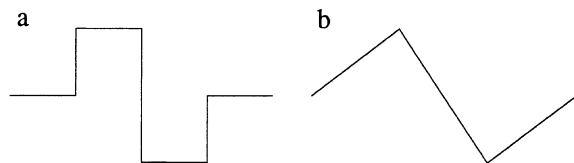


Fig. 6. The fundamental motifs for (a) the basic Minkowski fractal, and (b) the Minkowski island fractal.

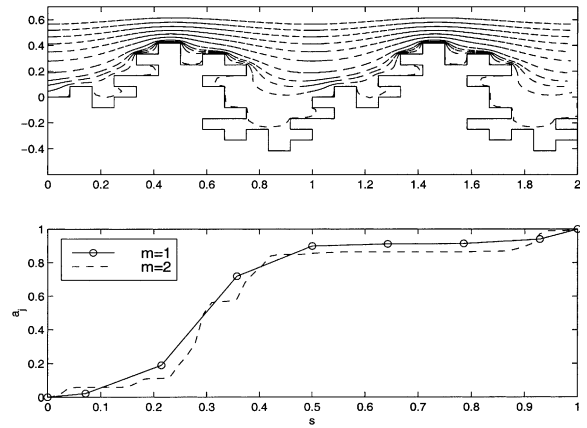


Fig. 7. Top: Minkowski pre-fractal  $m = 4$  and pattern of evenly spaced temperature contours. Bottom: dimensionless transport rates,  $a_j$ , at each vertex, each vertex,  $j = 1, \dots, N$  plotted against the cumulative arc length along the curve normalized by the total arc length.

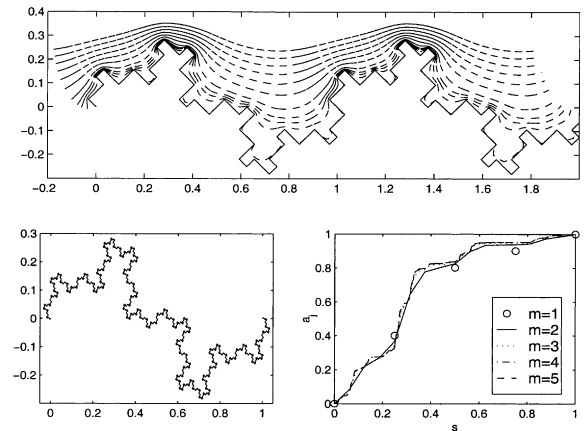


Fig. 8. Top: Minkowski island pre-fractal  $m = 3$  and pattern of evenly spaced temperature contours. Bottom left: Minkowski island  $m = 5$ . Bottom right: The corresponding dimensionless transport rates,  $a_j$ , at each vertex,  $j = 1, \dots, N$ , are plotted against the cumulative arc length along the curve normalized by the total arc length.

wall that rests just on top of the fractal, is monotonic for the Von Koch curve, but fluctuates for the Minkowski island fractal.

3.4. Random shapes

Models of wall roughness can be constructed by admitting a degree of randomness into the locations of the wall nodes. Keeping the end-vertices fixed, a single wall period can be generated by sampling the internal nodes randomly from a uniform distribution. Points

picked in this way for non-dimensional  $x \in (0, 1)$ ,  $y \in [-h, h]$  have a mean position  $(1/2, 0)$  and variances  $(1/12, h^2/2)$  in the respective directions. The points can then be sorted into order and joined up to create the wall. A better way to generate an irregular surface is to join up the random points directly and repeat the generation process until a non-intersecting wall has been found. This generation process allows the wall to double-back on itself, as shown in Fig. 9(a). Note that the presence of sharp crevices has little effect on the established temperature field. This observation is consistent with the Phragmén–Lindelöf theorem (e.g., [15]), which predicts exponential decay of a complex function in a sharp crevice. One pragmatic constraint of this approach is that the computational expense for simply generating the wall dramatically rises as the number of vertices increases. As a compromise, we generate an initial motif using a small number of random points, and then iterate  $m$  times to create a pre-fractal shape, as described in previous sections. Results for a sample random pre-fractal are displayed Fig. 9(b).

A run of 250 random walls with four vertices, each with dimensionless heights distributed between 0 and  $\sqrt{3}/4$ , yielded the average value  $\bar{c}_D = 0.1956$ , with a

standard deviation of 0.0879. This can be compared with the value 0.2654 for the first iteration of the Von Koch curve with four nodes. Another run of 250 random walls with the same variation in heights but 13 nodes produced the average value  $\bar{c}_D = 0.2916$ , with standard deviation 0.0419. This can be compared with the value 0.2970 for the second Von Koch iteration with 13 nodes. In both cases, the surface lengths averaged over all the random walls were comparable to those of the pre-fractals.

The random pre-fractal shown in Fig. 9(b) is only a small perturbation of the flat shape. The displacement constant is  $c_D = -0.0007$ , and the mean height of the curve is  $0.0002L$ . This would appear to be consistent with the perturbation analysis of Fyrrillas and Pozrikidis [4] for doubly-periodic walls, showing that, when the height of the corrugations is small compared to the wave length, the value of  $c_D$  is proportional to the average wall height. A run of a hundred random walls with  $h = 0.1$ , shown in Fig. 10(a), produced results that are consistent with the asymptotic analysis.

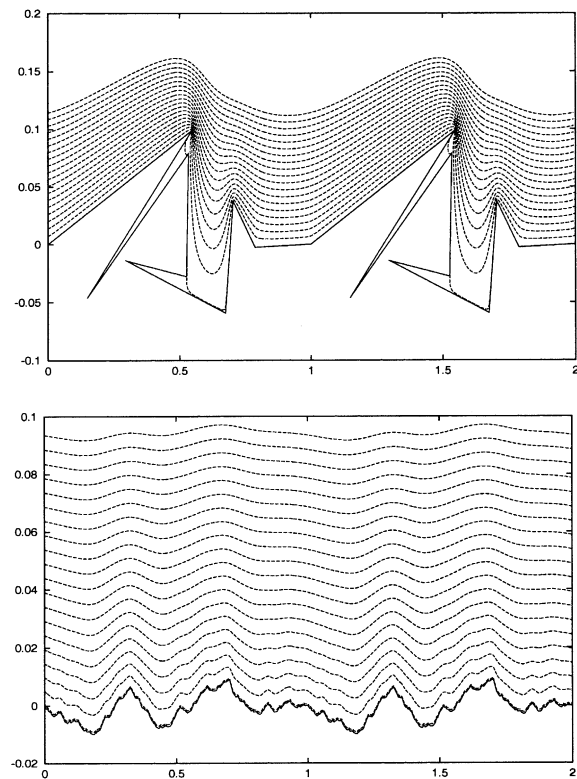


Fig. 9. Sample random walls. Top: Random wall with 10 vertices per period. Bottom: Pre-fractal wall with 344 nodes per period generated from a random motif. The dotted lines are evenly spaced temperature contours.

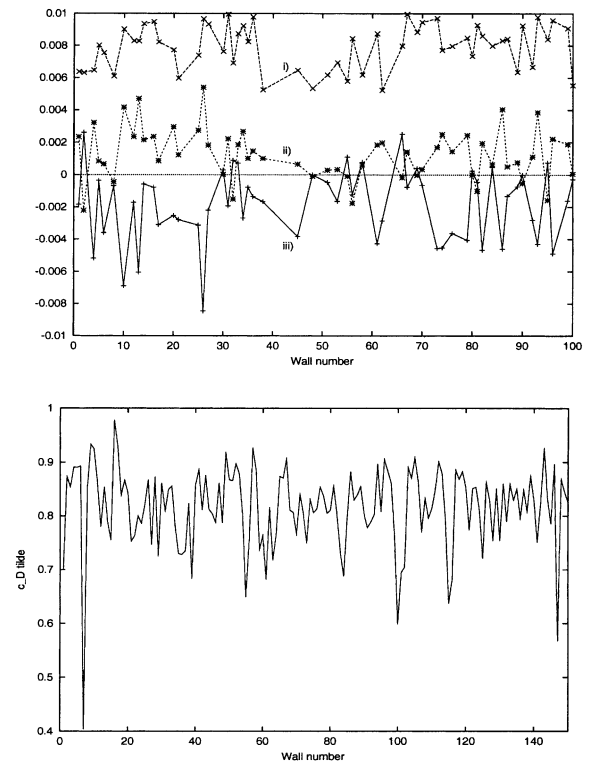


Fig. 10. Top: Computation for 100 random walls with five vertices per period and height  $h = 0.01$ . The three lines represent: (i) the maximum individual wall height, (ii) the mean individual wall height, and (iii)  $-c_D$ . Bottom: The modified displacement constant  $\bar{c}_D$  for 150 random walls with  $h = 1$  and five vertices per period. The displacement constant  $\bar{c}_D$  is bounded between 0 and 1, and its mean value is 0.8159.

Table 2  
Comparison of the two conformal mapping and boundary-integral method

$b$	0.222	0.444	0.666
$c_D$	0.127 (0.127)	0.143 (0.143)	0.160 (0.160)
$m$	1	2	3
$c_D$	0.176 (0.176)	0.173 (0.173)	0.174 (0.174)

Upper half:  $c_D$  for the triangular hump shown in Fig. 2 with asperity width  $b$ . Lower half:  $c_D$  for the first three iterates ( $m$ ) of the Von Koch curve. In each case the value computed using the conformal mapping technique is given, with that found by the boundary integral method shown in brackets.

Fig. 10(b) shows results for 150 random walls with five vertices and reduced height  $h = 1$ . To obtain a measure of the effect of the random corrugations in comparison to a flat wall of equivalent height, we compute the ratio  $\tilde{c}_D = (c_D + h_2)/(h_1 + h_2)$ . Recall that for a wall with maximum and minimum heights  $h_1L$  and  $-h_2L$ , the inequality  $-h_2 \leq c_D \leq h_1$  holds; accordingly,  $0 \leq \tilde{c}_D \leq 1$ . The scaled displacement constant  $\tilde{c}_D$  is the effective normalized  $c_D$  if the wall were shifted upwards so that its lowest point just touches the  $x$ -axis. For the walls displayed in Fig. 10(b),  $\tilde{c}_D$  has a mean value of 0.8159 with a standard deviation 0.0761. A further run of 150 random walls for  $h = 1$  with eight vertices produced a mean value of 0.8604 with a standard deviation of 0.0389. In line with what has been found for the fractal-like walls, including a higher number of vertices does not appear to have a significant effect on the rate of transport.

### 3.5. Double-layer formulation

To supply a check on the results computed using the conformal mapping method, we repeated some of the calculations using the boundary integral formulation discussed in Section 2.2. Specifically, the triangular protrusion shown in Fig. 2 and the Von Koch snowflake curve were reconsidered. For the former, the height of the asperity is taken to be  $1/(2\sqrt{3})$ , and  $c_D$  is computed for various widths  $b$ . For the fractal line, the first three iterations are examined. Table 2 shows calculated values of  $c_D$  using the two different techniques. The agreement is excellent in all cases.

## 4. Discussion

We have studied steady conductive heat transport in a two-dimensional semi-infinite domain bounded by a wall with piecewise-linear corrugations. Our chief aim has been to calculate the dimensionless displacement constant  $c_D$  regarded as a generic measure of the effect of wall irregularities. We have simulated the effects of

genuine wall roughness with simple pulse-like protrusions, and with both pre-fractal and random wall shapes, and presented results for intricate curves with up to 1025 vertices.

For any given shape, the geometrical inclusion theorem requires that  $c_D$  lie between the maximum and minimum wall heights. In the case of the regular protrusions, this means that the maximum value of  $c_D$  must occur when the asperities are so close together that they resemble a uniform wall, displaced by the protrusion height from the  $x$ -axis. However, this does not mean that the displacement constant must vary monotonically with decreasing asperity width, as was demonstrated in Fig. 4(b).

The effect of wall surface length does not seem to be so pronounced as might expected. For the regular protrusions, it appears that the shape plays a more important role than the total arc length, and the same holds true for the pre-fractal geometries. Although the surface length diverges with the iteration number, the displacement constant tends to a limit quite rapidly. Beyond a certain stage therefore, the introduction of further crenulations plays only a minor role.

In this paper, we have concentrated on two-dimensional solutions to the heat conduction equation. Spanwise variation has been considered recently by Fyrrillas and Pozrikidis [4] for symmetric doubly-periodic walls using the boundary-integral approach. Irregular or even random three-dimensional shapes have yet to be investigated.

## Acknowledgement

This research was supported by a grant provided by the National Science Foundation.

## Appendix A

In this Appendix A, we demonstrate that the value of the displacement constant  $c_D$  for a periodic wall is always less than that for another wall which envelops from above the first wall. Consider a fixed wall  $S_1$  on which  $T_1 = T_0$ , enclosing from above another boundary  $S_2$  on which  $T_2 = T_0$ . Both  $T_1$  and  $T_2$  are assumed to satisfy Laplace's equation throughout the region between the respective lower boundary and  $y = \infty$ . Let  $c_{D1}$  and  $c_{D2}$  be the displacement constants for the two walls. Starting from the reciprocal relation for harmonic functions we may write

$$\int_{\Omega} \nabla \cdot (T_1 \nabla T_2 - T_2 \nabla T_1) d\Omega = 0, \quad (\text{A.1})$$

over some arbitrary domain of integration  $\Omega$ . Take  $\Omega$  to be the area enclosed by a single period  $L$  of  $S_1$ , two vertical sides at  $x = 0$  and  $x = L$ , and a horizontal top at

$y = d$ , where  $d$  is sufficiently large for the asymptotic behavior of the harmonic functions to develop. Then, applying the divergence theorem and using the known asymptotic forms at infinity, (A.1) becomes

$$\int_{S_1} \left( T_0 \frac{\partial T_2}{\partial n} - T_2 \frac{\partial T_1}{\partial n} \right) ds = L^2 \gamma^2 (c_{D2} - c_{D1}), \quad (\text{A.2})$$

where  $\gamma = -q/\kappa$ ,  $s$  denotes arc length along the wall, and  $n$  is in the direction normal to  $S_1$  pointing into  $\Omega$ . The contributions from the vertical sides cancel due to the periodicity. Since  $\int_{S_1} \partial T_1 / \partial n ds = \int_{S_1} \partial T_2 / \partial n ds$  by heat conservation, we have

$$\int_{S_1} (T_0 - T_2) \frac{\partial T_1}{\partial n} ds = L^2 \gamma^2 (c_{D2} - c_{D1}). \quad (\text{A.3})$$

Now  $T_2$  is harmonic and must therefore attain its extreme value, namely  $T_0$ , on the boundary  $S_2$ . By a similar argument,  $\partial T_1 / \partial n$  must always be negative on  $S_1$ . Hence the integrand on the left hand side of (A.3) must be negative throughout the domain of integration. It follows that the integral itself is negative, which implies that  $c_{D2} < c_{D1}$ .

## References

- [1] G.P. Peterson, A. Ortega, Thermal control of electronic equipment and devices, *Adv. Heat Trans.* 20 (1990) 181–314.
- [2] M. Neagu, A. Bejan, Constructal placement of high-conductivity inserts in a slab: optimal design of roughness, *J. Heat Transf.* 123 (2001) 1184–1189.
- [3] A. Bejan, *Shape and structure from Engineering to Nature*, Cambridge University Press, Cambridge, UK, 2000.
- [4] M.M. Fyrillas, C. Pozrikidis, Conductive heat transport across rough surfaces and interfaces between two conforming media, *Int. J. Heat Mass Transf.* 44 (2001) 1789–1801.
- [5] G.I. Taylor, A model for the boundary condition of a porous material, Part 1, *J. Fluid Mech.* 49 (1971) 319–326.
- [6] S. Richardson, A model for the boundary condition of a porous material, Part 2, *J. Fluid Mech.* 49 (1971) 327–336.
- [7] B.B. Mandelbrot, *The Fractal Geometry of Nature*, W.H. Freeman, New York, 1982.
- [8] M. Brady, C. Pozrikidis, Diffusive transport across irregular and fractal walls, *Proc. Roy. Soc. Lond. A* 442 (1993) 571–583.
- [9] A. Majumdar, C.L. Tien, Fractal network model for contact conductance, *J. Heat Transf.* 113 (1991) 516–525.
- [10] J.M. Floryan, Conformal-mapping-based coordinate generation method for channel flows, *J. Comp. Phys.* 58 (1985) 229–245.
- [11] J.M. Floryan, Conformal-mapping-based coordinate generation method for flows in periodic configurations, *J. Comp. Phys.* 62 (1986) 221–247.
- [12] R.T. Davis, Numerical methods for coordinate generation based on the Schwarz–Christoffel transformations. In *Proc. 4th Am. Inst. Aero. Astro. CFD Conf.* Williamsburgh, Virginia, 1979.
- [13] D. Owen, B.S. Blatt, On flow through porous material using a generalized Schwarz–Christoffel theory, *J. Appl. Phys.* 71 (1992) 3174–3180.
- [14] C. Pozrikidis, Shear flow over a particulate or fibrous plate, *J. Eng. Math.* 39 (2001) 3–24.
- [15] G.F. Carrier, M. Krook, C.E. Pearson, *Functions of a complex variable*, McGraw-Hill, New York, 1966.
- [16] M. Abramowitz, I.A. Stegun, *Handbook of Mathematical Functions*, Dover, New York, 1965.
- [17] C. Pozrikidis, *Numerical computation in Science and Engineering*, Oxford University Press, Oxford, 1998.
- [18] C. Pozrikidis, *A Practical Guide to Boundary Element Methods; with the software library BEMLIB*, CRC Press, Boca Raton, Florida, 2002.
- [19] M.A. Lavrentev, B.A. Shabat, *Theoretical Methods of Functions of Complex Variables*, Nauka, Moscow, 1965 (in Russian).
- [20] H. Lauwerier, *Fractals*, Princeton Science Library, Princeton, 1991.